RESEARCH ARTICLE

Remodeling of the Z-Ring Nanostructure during the *Streptococcus pneumoniae* Cell Cycle Revealed by Photoactivated Localization Microscopy

Maxime Jacq, Virgile Adam, Dominique Bourgeois, Christine Moriscot, Anne-Marie Di Guilmi, Thierry Vernet, Cécile Morlot

University of Grenoble Alpes, IBS, Grenoble, France; CNRS, IBS, Grenoble, France; CEA, IBS, Grenoble, France

ABSTRACT **Ovococci form a morphological group that includes several human pathogens (enterococci and streptococci). Their shape results from two modes of cell wall insertion, one allowing division and one allowing elongation. Both cell wall synthesis modes rely on a single cytoskeletal protein, FtsZ. Despite the central role of FtsZ in ovococci, a detailed view of the *in vivo* nanostructure of ovococcal Z-rings has been lacking thus far, limiting our understanding of their assembly and architecture. We have developed the use of photoactivated localization microscopy (PALM) in the ovococcus human pathogen *Streptococcus pneumoniae* by engineering spDendra2, a photoconvertible fluorescent protein optimized for this bacterium. Labeling of endogenously expressed FtsZ with spDendra2 revealed the remodeling of the Z-ring's morphology during the division cycle at the nanoscale level. We show that changes in the ring's axial thickness and in the clustering propensity of FtsZ correlate with the advancement of the cell cycle. In addition, we observe double-ring substructures suggestive of short-lived intermediates that may form upon initiation of septal cell wall synthesis. These data are integrated into a model describing the architecture and the remodeling of the Z-ring during the cell cycle of ovococci.**

IMPORTANCE **The Gram-positive human pathogen *S. pneumoniae* is responsible for 1.6 million deaths per year worldwide and is increasingly resistant to various antibiotics. FtsZ is a cytoskeletal protein polymerizing at midcell into a ring-like structure called the Z-ring. FtsZ is a promising new antimicrobial target, as its inhibition leads to cell death. A precise view of the Z-ring architecture *in vivo* is essential to understand the mode of action of inhibitory drugs (see T. den Blaauwen, J. M. Andreu, and O. Monasterio, Bioorg Chem 55:27–38, 2014, doi:10.1016/j.bioorg.2014.03.007, for a review on FtsZ inhibitors). This is notably true in ovococcoid bacteria like *S. pneumoniae*, in which FtsZ is the only known cytoskeletal protein. We have used superresolution microscopy to obtain molecular details of the pneumococcus Z-ring that have so far been inaccessible with conventional microscopy. This study provides a nanoscale description of the Z-ring architecture and remodeling during the division of ovococci.**

Received 3 July 2015 **Accepted** 22 July 2015 **Published** 18 August 2015

Citation Jacq M, Adam V, Bourgeois D, Moriscot C, Di Guilmi A-M, Vernet T, Morlot C. 2015. Remodeling of the Z-ring nanostructure during the *Streptococcus pneumoniae* cell cycle revealed by photoactivated localization microscopy. mBio 6(4):e01108-15. doi:10.1128/mBio.01108-15.

Editor Caroline S. Harwood, University of Washington

Address correspondence to Cécile Morlot, cecile.morlot@ibs.fr, or Virgile Adam, virgile.adam@ibs.fr.

The tubulin homologue FtsZ is the major bacterial cytoskeleton protein. *In vivo*, it forms 4- to 5-nm-thick and 40- to 120-nm-long filaments (1, 2) that assemble into an annular structure called the Z-ring, which is positioned at midcell underneath the cytoplasmic membrane and is required for cytokinesis. Filament turnover relies on polymerization/depolymerization cycles, during which GTP binding triggers head-to-tail association of FtsZ subunits and GTP hydrolysis causes dissociation of the polymers (3). These filaments act as scaffolding elements for the recruitment of various division proteins, including proteins in charge of FtsZ association with the cytoplasmic membrane, FtsZ filament organization, cell wall growth and remodeling, chromosome dimer resolution, membrane fission, and cell separation (3–5).

Beyond having a scaffolding function, FtsZ is most likely involved in the generation of the constrictive force required for cytokinesis (3). One model proposes that the Z-ring undergoes constriction through a sliding motion between FtsZ filaments (6, 7). Another model proposes that continued constriction arises from the combination between FtsZ polymerization/depolymerization cycles and membrane bending induced by the curvature of nucleotide-bound FtsZ filaments (8–11). This model does not exclude the contribution of cell wall synthetic and remodeling enzymes to cytokinesis. Indeed, it is likely that the septal ingrowth of the cell wall pushes against the cytoplasmic membrane, contributing to the force required for invagination and to the stabilization of small local membrane constrictions (2, 12). Conversely, the constriction of FtsZ filaments will likely influence the kinetics of cell wall remodeling.

An important aspect of these models remains largely uncertain, namely, the structure adopted *in vivo* by FtsZ filaments at the nanoscale level. For many years since its initial observation by conventional fluorescence microscopy (13), the FtsZ macromolecular assembly has been modeled as a closed ring. Two electron cryotomography studies performed on *Caulobacter crescentus* and *Escherichia coli* cells provided controversial data, one showing loosely scattered bands of FtsZ protofilaments that support a

model in which the Z-ring is discontinuous (2) and the other showing filament doublets that support the closed-ring hypothesis (7). In parallel, photoactivated localization microscopy (PALM) experiments performed with *E. coli* and *C. crescentus* suggested that the Z-ring displays regions of varied densities and that the high-density regions are made of heterogeneous clusters of stationary, and therefore most likely polymerized, FtsZ molecules (14–16). In addition, these studies suggested that the FtsZ filaments most likely adopt a loose and overlapping three-dimensional (3D) arrangement in the high-density regions. Finally, 3D structured illumination microscopy (SIM) showed that the Z-rings in *Bacillus subtilis*, *Staphylococcus aureus*, and *Streptococcus pneumoniae* display a bead-collar-like structure, with the beads representing regions of high densities of FtsZ molecules (17, 18). All these studies suggest that the Z-ring might not form a packed and continuous ring but might rather be made of a heterogeneous arrangement of loose protofilament clusters. However, many questions remain open, in particular regarding the rearrangement of the filament clusters and the remodeling of the Z-ring throughout the division cycle. Recently, a high-throughput PALM study has allowed imaging of the nanostructure of the Z-ring at different stages of the *C. crescentus* cell cycle (19). Very few continuous rings were observed at all stages of the cell cycle, thus supporting a model in which the Z-ring is made of sparsely distributed patches of FtsZ filaments throughout the cell division process. In addition, the axial and radial thicknesses of the Z-ring were found to be approximately constant during constriction, with mean values of 71 nm and 64 nm, respectively.

These first superresolution studies provided important insights into the *in vivo* organization of the Z-ring, but the understanding of the general mechanisms of assembly and constriction now requires a nanoscale description of the Z-ring in other bacterial morphogenetic models.

Ovococci form a morphological group that includes several human pathogens (enterococci and streptococci). Their shape results from two modes of cell wall insertion, one allowing division by synthesizing a cross wall perpendicular to the main axis of the cell (septal synthesis) and another one allowing limited elongation by synthesizing the cell wall in restricted regions flanking the division site (peripheral synthesis). Since MreB is absent in ovococcal bacteria, both the division and the elongation machineries rely on the Z-ring to position the sites of cell wall synthesis at midcell (20, 21). Despite the central role of the Z-ring in ovococci, little is known regarding its architecture. The pneumococcal Z-ring appears as a bead-like single ring by 3D SIM (17, 22, 23), but we still lack structural details at the nanoscale level to understand how it controls the scaffolding of the growth and division machineries throughout the cell cycle.

Here, we report the investigation by PALM of the nanostructure of FtsZ in the ovococcal human pathogen *S. pneumoniae*. After modification of the photoconvertible fluorescent protein (PCFP) Dendra2, we imaged the Z-ring nanostructure at different stages of the bacterial cell cycle, using a strain expressing a single copy of FtsZ labeled at the native locus. In support of previous observations of bacteria with different shapes (2, 16, 18, 19), our images show that the Z-ring in ovococci is made of heterogeneous clusters of protofilaments at the division site. Our data also reveal a previously uncharacterized dynamic axial rearrangement of the Z-ring during constriction and the presence of double septal Z-rings in a fraction of the cell population. These observations are integrated into a model describing the nanostructural progression of the Z-ring throughout the pneumococcal cell cycle.

RESULTS

Engineering of a functional FtsZ-Dendra2 fusion for *S. pneumoniae*. To preserve interactions between FtsZ's C-terminal region and its partners (4, 24, 25), we first tested the expression of an FtsZ N-terminal fusion to the PCFP Dendra2. Dendra2 emits green fluorescence before photoconversion, a property that allowed checking its expression by epifluorescence before starting the PALM experiments. In addition, Dendra2 is monomeric, which induces minimal perturbations to the labeled target, and displays low blinking levels (26, 27), which facilitates accurate counting of single molecules.

In order to minimally impact the Z-ring assembly and decorate the ring with only a few fluorescent markers, Dendra2-FtsZ was first expressed under the control of a zinc-inducible promoter at the ectopic site of *bgaA* in *S. pneumoniae*. As illustrated in Fig. 1A, no signal could be detected using epifluorescence. Analysis of the expression level of Dendra2-FtsZ showed that it was expressed at levels too low to be measured by immunodetection (Fig. 1B). To solve this problem, we designed a synthetic Dendra2 gene harboring codons optimized for expression in *S. pneumoniae* (the spDendra2 gene) (see Fig. S1A in the supplemental material). In addition, we replaced the N and C termini of Dendra2 with the N and C termini of the green fluorescent protein (GFP) (Fig. S1B), a strategy known to confer better stability to red fluorescent proteins of anthozoan origin (28). Efficient expression of the fusion protein between FtsZ and spDendra2 (spDendra2-FtsZ) was revealed by Western blotting (Fig. 1B) and confirmed by the observation of a bright fluorescence signal localized at the *S. pneumoniae* division site (Fig. 1A). The similarity between the localization patterns of spDendra2-FtsZ and GFP^+-FtsZ (29) and FtsZ immunolocalization patterns (30) suggests that the N-terminal spDendra2 label does not impair the localization pattern of FtsZ. However, attempts to delete the native *ftsZ* gene in this strain failed, most probably because the expression level of ectopic spDendra2-FtsZ is too low to complement an *ftsZ* deletion (Fig. 1B).

We then considered designing an N-terminal spDendra2-FtsZ fusion at the native *ftsZ* locus under the control of the native promoter. The reporting of a functional endogenous C-terminal FtsZ-GFP^+ fusion by Fleurie and company (31) prompted us to instead construct a strain expressing a C-terminal FtsZ-spDendra2 fusion. This endogenous FtsZ-spDendra2 fusion displays a septal fluorescence signal that is very homogeneous among the pneumococcal population (Fig. 2A), and immunodetection was used to show that the levels of FtsZ-spDendra2 expressed were similar to endogenous levels in wild-type cells (Fig. S1C). In addition, the wild-type growth rate and cell length distributions (Fig. S1D and E) displayed by this strain indicate that the endogenous FtsZ-spDendra2 fusion assembles as a contractile ring, does not impair the cell division process, and is therefore functional.

spDendra2 is a functional PCFP for PALM studies of *S. pneumoniae*. PALM images were collected under wide-field illumination of fixed and live pneumococcal cells expressing FtsZ-spDendra2 (see Fig. S2 in the supplemental materials and see details in Materials and Methods below). We obtained an average localization precision of 22 ± 3 nm, and the spatial resolution of

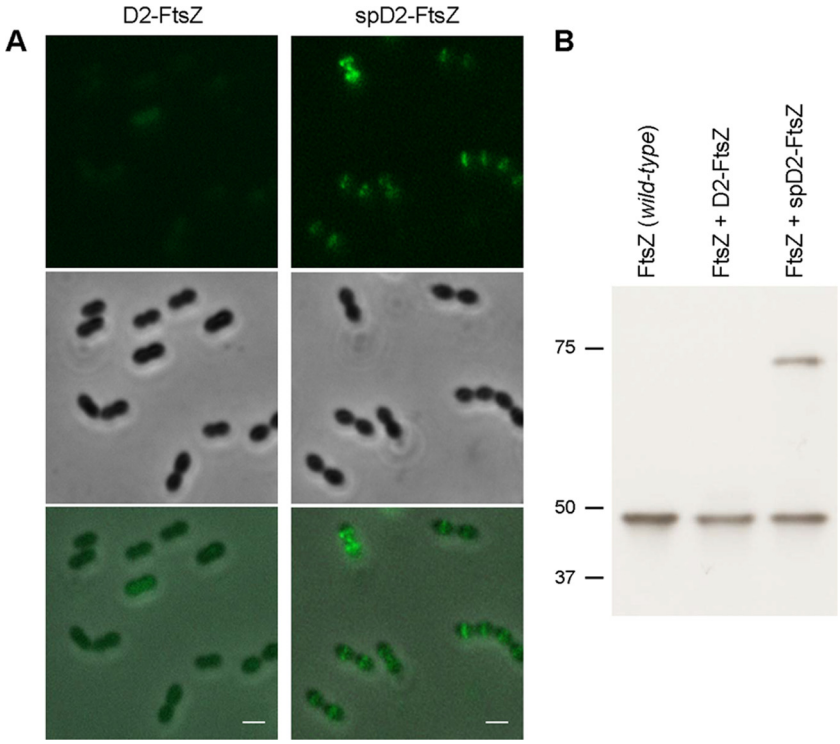

FIG 1 Development of spDendra2 for PALM studies of *S. pneumoniae*. Live cells expressing the ectopic Dendra2-FtsZ (D2-FtsZ) or spDendra2-FtsZ (spD2-FtsZ) fusions were visualized at an OD_{600} of 0.3 using conventional microscopy. Dendra2 and spDendra2 green epifluorescence, phase-contrast, and merged images are shown. Scale bars = 1 μm. (B) Expression levels of native FtsZ (FtsZ) and of ectopic Dendra2-FtsZ (D2-FtsZ) and spDendra2-FtsZ (spD2-FtsZ) fusions in strains R6 (left lane), spCM18 (middle lane), and spCM72 (right lane). Samples of cultures were harvested at an OD_{600} of 0.3 for the preparation of protein extracts. Equivalent amounts of total proteins for each sample were separated by SDS-PAGE, blotted to membranes, and analyzed by immunoblotting using anti-FtsZ serum. Positions of molecular mass markers are indicated by the numbers (in kilodaltons) to the left of the blots.

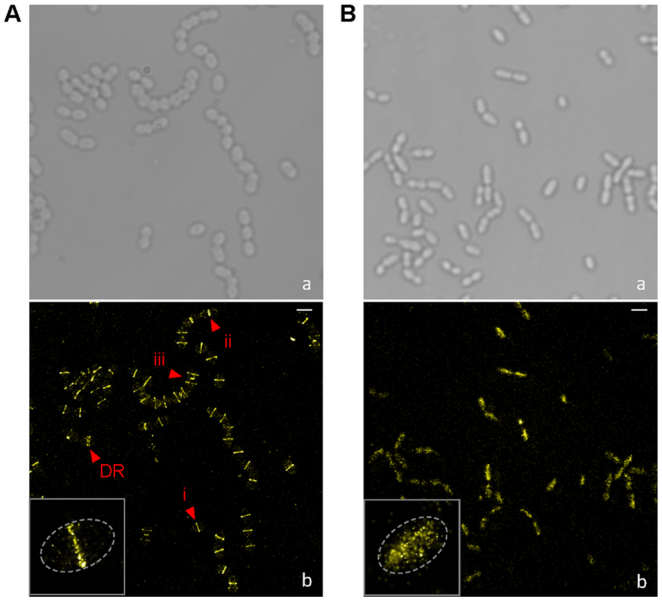

FIG 2 FtsZ displays specific septal patterns in fixed *S. pneumoniae* cells. Pneumococcal cells expressing an endogenous FtsZ-spDendra2 fusion (spMJ40) (A) or free spDendra2 in their cytoplasm (spMJ33) (B) were fixed and imaged at an OD_{600} of 0.3. Bright fields (a) and reconstructed PALM images (b) are shown. Red arrowheads point at cells in one of the three stages described in Fig. 3 or at a cell displaying a double ring (DR) of FtsZ as illustrated in Fig. 6. Gray-boxed inset images are 5-fold magnifications of one predivisional PALM pattern displayed in panel b. Dashed gray lines represent the periphery of the cell. Scale bars = 2 μm.

the reconstructed PALM images was estimated to be ~38 nm (Nyquist-limited resolution).

In order to determine the counting efficiency of spDendra2 fused to FtsZ, we measured the total amount of FtsZ molecules using immunodetection and compared it to the average number of FtsZ-spDendra2 molecules imaged by PALM. Using immunodetection (Fig. S2E), FtsZ was found to be present at 3,500 ± 800 molecules per cell, which is in the same range as the ~3,000 molecules previously reported for *S. pneumoniae* Rx1 (32). Quantitative analysis of the PALM images provided an average number of 670 ± 240 imaged molecules per cell (n = 217). The ratio of imaged FtsZ-spDendra2 molecules with respect to the estimated cellular copy number is therefore ~20%, which can be accounted for by limited photoconversion efficiency, residual protein misfolding, or improper chromophore maturation in the anaerobic *S. pneumoniae* bacterium (33, 34). Overall, these results demonstrate that spDendra2 is a PCFP well suited for PALM studies of *S. pneumoniae*.

Pneumococcal FtsZ displays specific patterns throughout the cell cycle. The Z-ring is a highly dynamic structure undergoing constant renewal due to the rapid exchange between polymerized FtsZ molecules assembled in the ring and monomeric FtsZ molecules (14, 35–37). In order to trap and visualize Z-ring nanostructures at all stages of cell division, including hypothetical structures of a short-lived nature, we fixed ensembles of pneumococcal cells growing asynchronously and collected PALM images. The homogeneous labeling provided by the endogenous FtsZ-spDendra2

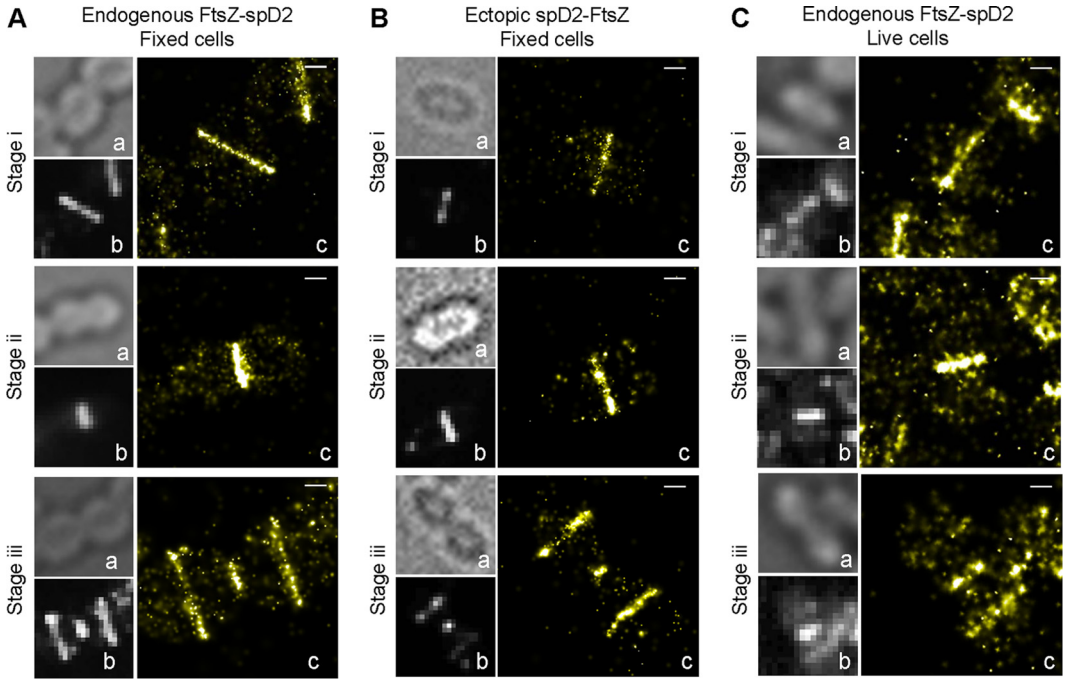

FIG 3 PALM images of representative patterns of the Z-ring throughout the pneumococcal cell cycle. Typical pneumococcal cells expressing the endogenous FtsZ-spDendra2 fusion (spMJ40) (A and C) or the ectopic spDendra2-FtsZ fusion (spCM72) (B) were classified into three stages defined by the diameter of the Z-ring, the cell length, and the distributions of FtsZ at the division site of the mother cell and the division sites of the two daughter cells. Cells were either fixed (A and B) or directly imaged (C) at an OD_{600} of 0.3. Bright-field (a), diffraction-limited (b), and reconstructed PALM (c) images are shown. Scale bars = 250 nm.

fusion over the whole pneumococcal population (Fig. 2A) indicated that our fixation conditions preserved Z-ring assembly at midcell and allowed us to extract meaningful data at all stages of the cell cycle. Importantly, cells expressing free spDendra2 (Fig. 2B) did not show enriched fluorescence signals at midcell, confirming that the structured patterns observed in cells expressing the fused version specifically result from the assembly of FtsZ into Z-rings.

Based on the measurement of the Z-ring diameter and FtsZ-spDendra2 localization, we classified the pneumococcal cells into three classes representative of the main FtsZ PALM patterns observed throughout the cell cycle (Fig. 3A and S3). The first class (stage i), which represents 57% of the entire cell population (n = 217), corresponds to cells that do not show apparent constriction in bright-field images and cells in which the Z-ring displays a diameter ranging from 1,200 to 700 nm. In this category of cells, the ring displays a heterogeneous FtsZ distribution. The second class (stage ii, 24% of the cell population) contains cells showing a clear constriction in bright-field images and cells in which the Z-ring displays a diameter ranging between 800 and 450 nm. At this stage, the Z-ring appears brighter, less heterogeneous, and thicker. In the third class (stage iii, 15% of the cell population), FtsZ molecules disassemble from the parental division site and start reassembling at the division sites of the future daughter cells. The diameter of the parental Z-ring in these cells is smaller than 450 nm. At stage iii, the FtsZ clusters become visible again in the parental ring and the two new Z-rings assembling at the future division sites of the daughter cells look similar to those observed at stage i. Finally, 4% of the cells surprisingly display double Z-rings, which will be described in a separate section.

Consistently with the idea that the presence of the spDendra2 label does not impair the structure of the Z-ring, the same PALM nanostructures could be visualized when the native Z-ring was decorated with the ectopic spDendra2-FtsZ fusion (Fig. 3B and S4A). Similar PALM nanostructures were also observed in live pneumococcal cells (Fig. 3C and S4B), indicating that the patterns observed in fixed cells were not significantly modified by paraformaldehyde fixation.

A quantitative analysis of our PALM data show that, at stage i, the total number of imaged FtsZ-spDendra2 molecules per cell (n = 125) was 600 ± 200, while 300 ± 60 molecules were imaged at midcell. At stage ii, the total number of FtsZ-spDendra2 molecules and the number of septal FtsZ-spDendra2 molecules imaged per cell (n = 51) were estimated to be 700 ± 250 and 300 ± 80, respectively. Assuming a homogeneous efficiency of counting of spDendra2 molecules throughout the imaging field of view, we conclude that about 50% and 42% of FtsZ molecules are present in the ring at stages i and ii, respectively. Due to the ovoid shape of the pneumococcus, the majority of the cells lie along their longitudinal axis, with the septal plane perpendicular to the microscope slide. Most of the Z-rings are therefore imaged on their side, and the observed patterns result from the 2D projection of the ring along the radial axis of the pneumococcal cells, obscuring the exact FtsZ distribution. Thus, the number of detected molecules in these rings might be underestimated by the fact that the diameter of the Z-rings at stage i is larger than the depth of field (DOF) of our microscope objective (<700 nm).

Pneumococcal FtsZ forms a clustered ring-like structure at midcell. At all stages of the cell cycle, the PALM images reveal an irregular Z-ring structure made of large regions displaying high fluorescence intensity alternating with regions of low fluorescence intensity (Fig. 3 and 4A, and see Fig. S3 and S5 in the supplemental

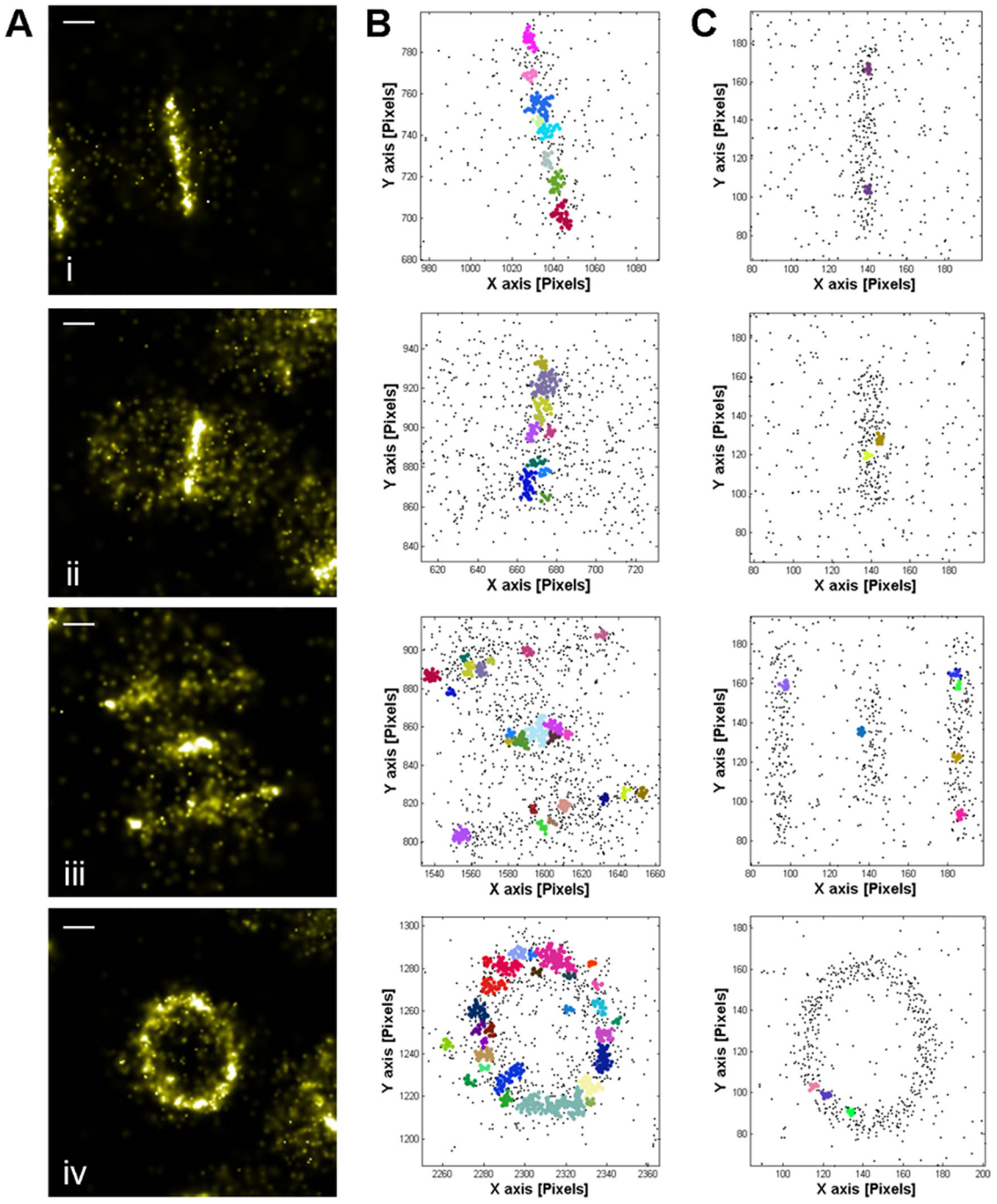

FIG 4 The pneumococcal Z-ring is made of heterogeneous clusters. (A) Reconstructed PALM image of the Z-ring in fixed cells expressing the endogenous FtsZ-spDendra2 fusion at stages i, ii, and iii or in a tilted orientation (iv). Scale bars = 250 nm. (B) Cluster analysis of the PALM images shown in panel A using the DBSCAN algorithm (38). Different colors are used to visualize the different clusters. Nonclustered molecules are shown as black dots. (C) Cluster analysis of simulated PALM imaging of continuous and homogeneous Z-rings. The cluster diameter threshold was set at 22 nm.

material). Cluster analysis of stages i to iii using DBSCAN (38) shows the presence of FtsZ clusters within the ring at all stages of constriction (Fig. 4B). To get a more accurate view of these FtsZ clusters, we took advantage of the tilted orientation of some chained cells, in which we could observe tilted Z-rings (Fig. 4A, panel iv, and Fig. S5). The diameter of the Z-ring in all these cells is larger than 800 nm, indicating that they belong to predivisional stage i. These tilted cells allow observation of Z-rings in a pseudo-3D manner at a resolution that exceeds that typically featured by 3D PALM using, e.g., the astigmatism method (39). In addition, the Z-ring shown in Fig. 4A (panel iv) is tilted by around 90° and is therefore completely encompassed within the depth of field of our microscope objective. Cluster analysis of this tilted Z-ring using DBSCAN indicates that it contains 28 FtsZ clusters

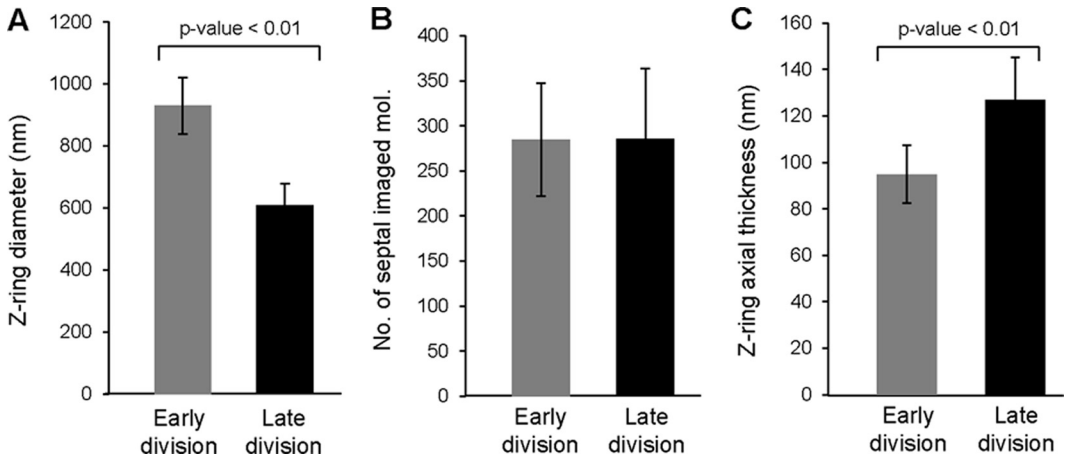

FIG 5 The Z-ring's axial thickness increases during constriction. (A) Mean values for the Z-ring diameter (A), the number of imaged septal FtsZ molecules (B), and the Z-ring's axial thickness (C) are reported for fixed cells in the early (Z-ring diameter > 800 nm [dark gray]) or late (Z-ring diameter <700 nm [black]) divisional stage. During constriction, the Z-ring's axial thickness increases by ~32 nm while the number of imaged FtsZ-spDendra2 molecules at the division site shows no significant variation. Error bars represent standard deviation values.

(Fig. 4B), in which between 7 and 135 FtsZ-spDendra2 molecules are imaged. On the other hand, the low-intensity regions and the cytoplasm contain discrete molecules. DBSCAN analysis of the Z-rings that are tilted by less than 90° (Fig. S5) indicates that they contain similar densities of clusters, except in regions located outside the depth of field of the objective.

In order to exclude the hypothesis that the observed granular arrangement of the Z-ring results from a reconstruction artifact, we simulated PALM images of spDendra2 molecules homogeneously distributed within areas representing 2D projections of Z-rings typical of cells at stages i, ii, and iii or viewed in a tilted orientation. A copy number of spDendra2 molecules equivalent to the experimental mean number of imaged molecules in the rings was used, and the simulation took into account multiple factors that influence the final PALM images, including the fluorescence background level and the photophysical behavior of spDendra2 that we extracted from the real data (26). Cluster analysis of the simulated PALM images using DBSCAN parameters equivalent to the ones that we used to analyze the experimental data show the quasi-absence of clusters in the simulated reconstructed rings (Fig. 4C). Thus, we conclude that the experimental FtsZ clusters imaged in the pneumococcal Z-rings are most likely real.

The pneumococcal Z-ring thickens during constriction. Interestingly, during late division, when the Z-ring shows a clear constriction, the Z-ring appears thicker, brighter, and more homogeneous than during early division (Fig. 3, 4, and S3). We can, however, still visualize FtsZ clusters at this stage (Fig. 4B).

We measured the axial thickness of the Z-ring in cells at early (Z-ring diameter larger than 800 nm) and late (Z-ring diameter smaller than 700 nm) division stages (Fig. 5A). We obtained mean axial thickness values of 95 ± 12 nm (n = 65) and 127 ± 18 nm (n = 64) for early and late divisional Z-rings, respectively (Fig. 5C), revealing a 32-nm thickening of the ring upon constriction. The number of imaged septal FtsZ-spDendra2 molecules in early and late divisional cells (300 ± 60 and 300 ± 80, respectively) (Fig. 5B) indicates that neither the higher brightness nor the increased axial thickness of the Z-ring at stage ii is due to the recruitment of additional FtsZ-spDendra2 molecules.

Based on Z-ring dimensions (Fig. 5A and C), we calculated the area of the 2D projection of the Z-ring along the radial axis and obtained mean area values of ~90 × 10^3 nm^2 and ~80 × 10^3 nm^2 for early and late division rings, respectively. This observation indicates that despite the 32-nm increase of the Z-ring thickness, the area of the 2D projection of the ring decreases during constriction, which is why the Z-ring appears brighter at stage ii.

FtsZ displays double-ring patterns. Unexpectedly, 4% of cells in the reconstructed PALM images display double Z-rings at midcell (Fig. 6 and S6A), separated by variable distances, ranging from ~50 to ~300 nm, with an average distance of 164 ± 72 nm (n = 16). The absence of curvature of the double rings and the lack of signal connecting them indicate that they do not correspond to the two halves of tilted Z-rings. In order to determine whether double rings result from artifactual step motions of the cells during data collection, we split the PALM data set into two consecutive subsets and reconstructed the corresponding PALM images. The double Z-rings could be visualized in the two data subsets, indicating that they correspond to a real localization pattern of FtsZ. Double Z-rings could be observed in fixed and live cells expressing the endogenous FtsZ-spDendra2 fusion or the ectopic spDendra2-FtsZ fusion (Fig. 6A to C), suggesting that they are due neither to a fixation artifact nor to a loss of function caused by C- or N-terminal fusions of spDendra2 to FtsZ. Overall, the double Z-rings may result from a biologically significant assembly of two spatially separated Z-rings at midcell.

We never observed any double Z-ring at the peripheral sites of stage iii cells. In addition, the observed cells do not show any visible constriction and the double Z-rings display diameters of 850 ± 100 nm (Fig. S6B). A total number of 300 ± 90 FtsZ-spDendra2 molecules were imaged in the double Z-rings (Fig. S6C), indicating that, overall, they contain the same amount of FtsZ molecules as single predivisional rings. These observations suggest that the double-Z-ring structures may correspond to short-lived intermediates between stages i and ii, possibly due to splitting of the initial Z-ring.

DISCUSSION

We have employed PALM to study the nanostructure of FtsZ in a pathogenic ovococcoid bacterium, *S. pneumoniae*. To that pur-

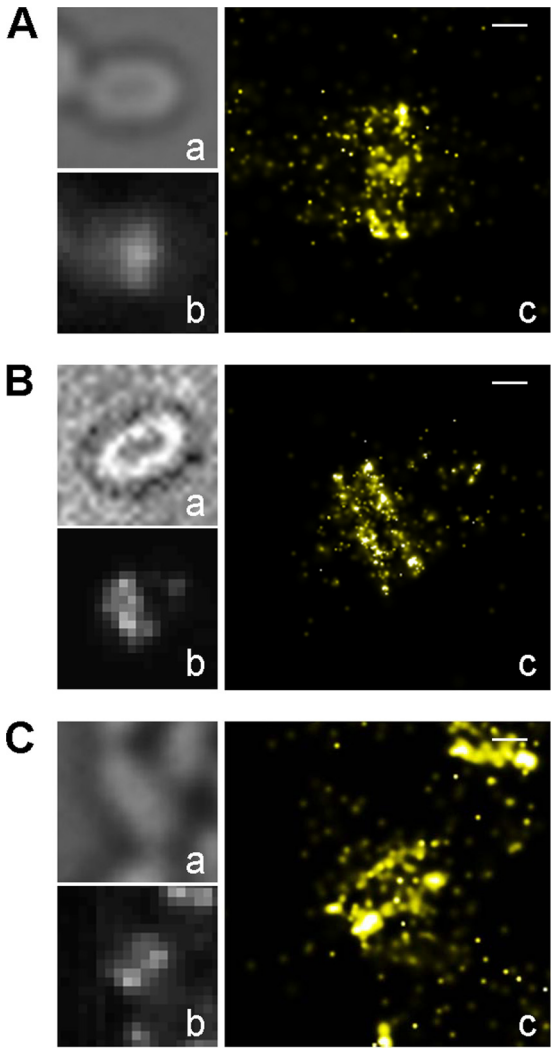

FIG 6 Pneumococcal FtsZ displays double-ring patterns. Pneumococcal cells expressing the endogenous FtsZ-spDendra2 fusion (spMJ40) (A and C) or the ectopic spDendra2-FtsZ fusion (spCM72) (B) were either fixed (A and B) or directly imaged (C) at an OD_{600} of 0.3. Bright-field (a), diffraction-limited (b), and reconstructed PALM (c) images are shown. Scale bars = 250 nm.

pose, we have designed spDendra2, a PCFP whose gene was codon optimized for this bacterium, and we have used a bacterial strain expressing a single copy of the endogenous *ftsZ* gene. Besides supporting a patchy band model for the assembly of FtsZ molecules at the division site, our data provide details into the remodeling of the Z-ring during the cell cycle of ovococci.

FtsZ forms heterogeneous clusters at midcell in bacteria with different shapes. Two main models have been proposed for the spatial organization of the Z-ring (12). The first one proposes that FtsZ molecules form a continuous ring at midcell. This model is supported by the capacity of FtsZ filaments to bundle *in vitro* and by the observation of continuous Z-rings reconstituted in artificial lipid tubules (7, 25, 40). The second model, called the "patchy band" or "bead-like" model, proposes that short FtsZ protofilaments are loosely arranged within discrete clusters at midcell. This model was suggested by 3D SIM experiments performed with *B. subtilis* and *S. aureus* and supported by PALM studies performed with *E. coli* and *C. crescentus* (16, 18, 19), but it has not been investigated in detail with ovococci. In addition, the large majority of these studies used merodiploid bacterial strains expressing the native copy of FtsZ and a fluorescently labeled ectopic copy, an experimental condition that may have induced division defects and led to the observation of structural artifacts. In our work, we have imaged in parallel the Z-ring in a merodiploid strain and in a strain expressing a single labeled FtsZ copy expressed at wild-type levels under the native FtsZ promoter. Our PALM images reveal the highly granular assembly of FtsZ, particularly visible in predivisional septal and peripheral Z-rings at stages i and iii, respectively, which is in contrast to the homogeneous and smooth appearance of the pneumococcal Z-ring usually obtained by conventional fluorescence microscopy (29). At stage ii of the cell cycle, FtsZ clusters are still present but are less dispersed within the ring. The similarity between the granular aspect obtained with the pneumococcal strains expressing the ectopic or the endogenous spDendra2-labeled FtsZ protein indicates that the clustered patterns of the Z-ring do not result from overexpression or malfunction of the FtsZ fusion proteins. Notably, in recent 3D SIM imaging of pneumococcal FtsZ, the heterogeneous fluorescence of the Z-ring appears in agreement with results of our PALM study (17, 22, 23). Our data argue against a model in which FtsZ molecules form a homogeneous and tightly packed ring and rather support the "patchy band" model. More generally, the coherence between our results, performed with an ovococcus model, and superresolution studies performed with two other bacterial morphological models (cocci and bacilli) indicates that the heterogeneous and clustered arrangement of the Z-ring throughout the cell cycle is conserved between species with different shapes and division modes. Of note, we never observed the helical patterns previously reported for the *E. coli* Z-ring (16).

Composition and assembly of a clustered pneumococcal Z-ring. The granular arrangement of the Z-ring in our PALM images is further supported by the fact that the septal region of a pneumococcal cell does not contain enough FtsZ molecules to allow the assembly of a tightly packed Z-ring of 95-nm width. Indeed, as estimated by immunoblotting (Fig. S2E), the strain that we used for our work expresses ~3,500 copies of the endogenous FtsZ-spDendra2 fusion protein, with ~50% (i.e., ~1,750 molecules) of them being located at midcell during early division. Given the 4-nm length of a subunit in an FtsZ filament (3) and the ~930-nm diameter of predivisional Z-rings in *S. pneumoniae* (Fig. 5B), 1,750 septal FtsZ molecules may form a continuous filament of 7,000-nm length, encircling the division site 2 to 3 times. Pneumococcal FtsZ polymerizes *in vitro* as 5-nm-wide filaments (Fig. S7 and Text S1). The width of 2 to 3 protofilaments arranged side by side as a monolayer therefore ranges between 10 and 15 nm, which is much lower than the average 95-nm value measured for the axial thickness of the predivisional Z-ring, even taking into account the broadening effect due to our ~38-nm resolution. Although it is not yet possible to calculate precisely how many protofilaments compose the Z-ring based on the measurement of its thickness, we can reasonably propose that the pneumococcal Z-ring cannot be made of homogeneously and tightly packed FtsZ filaments. Now that several studies performed with the three main morphological models (bacilli, cocci, and ovococci) have established that FtsZ assembles as a heterogeneous and clustered divisional ring, it will be important to determine the organization of the FtsZ filaments within the clusters. The fact that

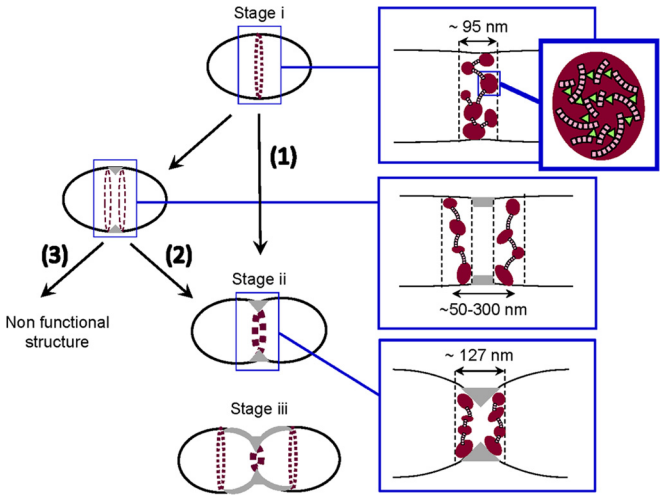

FIG 7 Model of the nanostructure of the Z-ring in the cell cycle of ovococci. At the onset of a division cycle, FtsZ molecules (represented as light-pink squares) polymerize and form heterogeneous clusters, which are distributed within an ~95-nm-thick ring-like structure (the so-called Z-ring) at midcell. Three alternative paths are then proposed. In the first path (1), the predivisional Z-ring directly proceeds to constriction. In the second path (2), the single predivisional ring duplicates into two functional rings that progressively separate as the cell wall is synthesized at the division site (interpeak distances ranging from 50 to 300 nm). Upon constriction, the distance separating the double Z-rings decreases, and the unresolved rings are eventually imaged as an ~127-nm-thick single ring at midcell. In both paths, the FtsZ molecules start disassembling from the parental division site at stage iii and two new predivisional Z-rings appear at the future division sites of the daughter cells. Each newborn daughter cell will eventually display a single stage i Z-ring. In the third path (3), double rings are not functional for division and they are potentially resolved by an unknown proofreading or stress response mechanism. Blue boxes frame regions that have been magnified to illustrate the heterogeneous and clustered arrangement of the Z-ring, the splitting of the predivisional Z-ring before constriction, and the thickening of the apparent single Z-ring at stage ii. Dimensions measured in this work are indicated. Purple-red areas represent regions with high FtsZ density (FtsZ clusters). These regions have been magnified to illustrate the presence of FtsZ filaments (pink rectangles), potentially connected by FtsZ partners (green triangles). Gray areas represent regions of cell wall synthesis.

tilted Z-rings display a homogeneous thickness along the periphery of the ring suggests that the radial diameter of the Z-ring is approximately of the same dimension as the axial diameter, within our ~38-nm resolution limit. This observation therefore supports a model in which FtsZ filaments assemble in both the axial and the radial dimension to form three-dimensional clusters (Fig. 7). The mechanism by which FtsZ clusters assemble remains to be deciphered. Lateral interactions between FtsZ filaments might participate in the formation of clusters, but so far, only doublets of FtsZ filaments have been detected *in vivo* (7). Alternatively, FtsZ-interacting proteins might establish connections between FtsZ filaments, thereby inducing cluster formation and stabilization. Among the dozen FtsZ-interacting partners that have been identified so far (25), only five (FtsA, SepF, ZapA, EzrA, and FtsEX) are conserved in *S. pneumoniae*. Some of these proteins may be involved in the assembly of pneumococcal FtsZ filaments into clusters.

The FtsZ clusters in our images are separated by low-density regions in which the concentration of FtsZ molecules is not significantly different from the cytoplasmic one. This observation suggests that the Z-ring might be discontinuous. However, because we imaged only 20% of the FtsZ molecules, we cannot exclude the possibility that the clusters are connected by very low concentrations of FtsZ filaments. In the future, it will be very interesting to determine the mechanism underlying the variations in FtsZ density within the ring.

Variation in the Z-ring nanostructure throughout the cell cycle in ovococci. Previous superresolution studies indicate that predivisional Z-rings in *E. coli* and *C. crescentus* display an axial thickness of ~110 and ~71 nm, respectively (16, 19). In pneumococcal predivisional cells, we observed Z-rings with an ~95-nm axial thickness. The difference between the values obtained for these three bacterial species with very different shapes suggests that the axial thickness of the Z-ring might be governed by physical constraints imposed by cell shape. Alternatively, proteins involved in the assembly and placement of the Z-ring might play an important role. *S. pneumoniae* is devoid of the canonical systems for Z-ring positioning, but recently, it was shown that the protein MapZ (midcell-anchored protein Z) forms ring structures at the cell equator before FtsZ and positions the Z-ring through direct protein-protein interactions (22, 41). Therefore, MapZ might have a role in the regulation of the Z-ring's thickness. On the other hand, the other positive FtsZ regulators (FtsA, ZapA, SepF, and FtsEX) may also be involved in the regulation of the Z-ring's dimensions.

Our data reveal that the axial thickness of the pneumococcal Z-ring increases by ~32 nm upon constriction. This variation is below the limit of the diffraction of light, which is why it has never been detected using conventional microscopy. Controversial data regarding the variation of the Z-ring dimensions throughout the *C. crescentus* cell cycle have been reported. While Biteen et al. reported an ~25-nm increase in the axial-Z-ring's thickness of one constricting cell (14), no variation was observed by Holden et al. (19), who performed their study on hundreds of cells. In *E. coli*, the dimensions of the Z-ring throughout the cell cycle have not yet been reported. Additional studies performed on different morphological groups of bacteria will be valuable to determine whether the thickening of the Z-ring during constriction is a general feature or is specific to ovococci.

The mechanism by which the pneumococcal Z-ring thickens upon constriction remains to be elucidated. It does not result from the additional recruitment of FtsZ molecules since the number of septal FtsZ molecules remains constant between stage i and stage ii, consistent with previous work from Strauss et al. showing that the amount of fluorescence remains constant during constriction in *B. subtilis* cells expressing an endogenous FtsZ-GFP fusion (18). Notably, this observation also indicates that the constriction of the Z-ring does not require the progressive loss of FtsZ molecules in the ring. On the other hand, the Z-ring width might increase to compensate for the decrease in its diameter, allowing the toroidal volume to remain constant. However, variations in toroidal volume cannot be discussed based on our PALM data because we could not observe any tilted Z-ring at stage ii of the cell cycle, and we therefore do not know whether the radial width of the Z-ring varies during constriction. An intriguing observation, which is the presence of double Z-rings in predivisional cells, might actually provide important clues regarding the mechanism through which the Z-ring thickens. This mechanism is discussed in the next section.

Pneumococcal FtsZ forms double rings. In 4% of the cells, we observed double Z-rings that were never reported for any other

bacterial species. These double Z-rings might represent abnormal localizations that assemble either randomly or in response to stress. These structures might then get corrected by a mechanism ensuring the assembly and stabilization of a single annular Z-ring at midcell, and this possibility is integrated in the model proposed in Fig. 7. StkP, GpsB, or MapZ might participate as such a proofreading mechanism, as cells expressing a deficient StkP or cells lacking GpsB or MapZ display aberrant FtsZ patterns (22, 31, 41, 42).

The double Z-rings observed here, however, display several characteristics supporting the hypothesis that they might be functional and constitute an intermediate step in constriction. First, they are the only atypical FtsZ localization patterns that we detected in our PALM images, while one might expect nonfunctional FtsZ assemblies to adopt more-various structures. Second, double rings are never observed at the equatorial positions of cells at stage iii. Third, the ~853-nm diameter of these double Z-rings is in the range of stage i predivisional ring diameters. Fourth, the total number of imaged FtsZ-spDendra2 molecules in the double rings corresponds to the number of molecules that are imaged in stage i single rings. Fifth, the distance separating the double rings ranges between ~50 and 300 nm, which fits in the ~300-nm distance separating the double rings of MapZ, the recently discovered FtsZ positioning protein (22). All together, these data suggest that the double Z-rings might correspond to a physiological intermediate structure, possibly building up just before constriction, between stage i and stage ii (Fig. 7). In this model, the predivisional single Z-ring (stage i) has to undergo splitting through a mechanism that remains to be deciphered. As was proposed for the splitting of the equatorial MapZ ring (22), initial cell wall synthesis performed by the division or the elongation machinery may allow splitting of the predivisional Z-ring and separation of the double rings.

Our model predicts that the axial thickness of the Z-ring in unconstricted cells should increase until the two rings are distinguishable and then decrease again as the two rings merge. The values obtained for the Z-ring's axial thickness and for the distance separating the double rings are in agreement with this prediction. Indeed, the axial thickness of the Z-ring in unconstricted cells ranges from ~75 to ~210 nm; this variability might therefore arise from the progressive separation or merging of unresolved rings. In addition, the double rings are separated by various distances (~50 to 300 nm), which potentially correspond to different stages in the separation or merging process. Finally, at stage ii of the cell cycle, we did not detect the presence of double Z-rings, possibly because they have merged or because the invagination of the cytoplasmic membrane has reduced the distance between the double Z-rings to a value below our resolution limit. The potential presence of unresolved double Z-rings at stage ii might explain why we see a thickening of the apparent single Z-ring at this stage. In our model, we therefore propose that the thickening of the Z-ring during constriction might result from the juxtaposition of two unresolved Z-rings.

In the future, PALM studies of the Z-ring in *mapZ* mutants, in mutants impaired for septal or peripheral cell wall synthesis, or in the presence of β-lactam antibiotics will be required to test our model and elucidate the mechanism of double-Z-ring formation and separation.

Conclusions. The nanostructural details provided in this work are consistent with a model (Fig. 7) in which, at the onset of the cell cycle, FtsZ filament clusters form an ~95-nm-thick ring-like structure stabilized by FtsZ-interacting partners and are potentially connected by low concentrations of FtsZ filaments. The observation of a double-Z-ring phenotype in a small fraction of the population suggests that the predivisional Z-ring might then separate into two rings, an event possibly induced by the initiation of cell wall synthesis at midcell. The two Z-rings would then come close to each other during constriction and eventually disassemble from the parental division site while two new predivisional Z-rings appear at the future division sites of the daughter cells. Alternatively, the double Z-rings might constitute a nonfunctional state that occurs either randomly or in response to stress. This work is a first step toward the elucidation of the remodeling mechanisms of the Z-ring throughout the cell cycle in ovococci. Further investigations will require imaging of the Z-ring in pneumococcal cells lacking or depleted of proteins involved in Z-ring assembly, stabilization, and positioning, such as FtsA, ZapA, SepF, EzrA, GpsB, or MapZ. Finally, the presented data on *S. pneumoniae* should motivate the use of PALM in other pathogenic cocci like enterococci or staphylococci.

MATERIALS AND METHODS

Bacterial strains and plasmids. Tables of strains, plasmids, and oligonucleotide primers and descriptions of their constructions can be found in Table S1 in the supplemental material. The spDendra2 synthetic gene was ordered from GeneArt Gene Synthesis (Life Technologies). Allelic replacements were performed using the Janus method as described previously (42). Briefly, we used a two-step procedure based on a bicistronic *kan-rpsL* cassette called Janus (43) to replace the *ftsZ* gene with the *ftsZ*-spDendra2 gene fusion form. This method avoids polar effects and allows expression of the fusion proteins at physiological levels.

Growth conditions, media, and bacterial transformation. Liquid cultures of *S. pneumoniae* strains were grown at 37°C in C medium supplemented with 0.5% yeast extract (CY) (44) or in Todd Hewitt medium (TH; BD Sciences). For strains harboring a zinc-inducible plasmid, CY was supplemented with 0.15 mM $ZnCl_2$ for expression of the fusion proteins. For transformation, ~250 ng of DNA was added to cells treated with synthetic competence stimulating peptide 1 in TH supplemented with 1 mM $CaCl_2$. Cells were grown for 2 h at 37°C, and transformants were selected on Columbia blood (4%) agar plates containing the appropriate antibiotics (tetracycline, 2.5 $\mu g \cdot ml^{-1}$; streptomycin, 200 $\mu g \cdot ml^{-1}$; or kanamycin, 250 $\mu g \cdot ml^{-1}$).

Immunoblot analysis. *S. pneumoniae* cells grown at 37°C in CY were harvested at an optical density at 600 nm (OD_{600}) of 0.3, concentrated 30-fold in Laemmli buffer supplemented with 20 $\mu g \cdot ml^{-1}$ DNase, and heated to 95°C for 5 min. Whole-cell extracts and dilutions of recombinant pneumococcal FtsZ (purified as described in the previous paragraph) were then loaded onto 12.5% polyacrylamide precast gels (Bio-Rad), resolved by SDS-PAGE, and electroblotted onto nitrocellulose membranes (Bio-Rad). Membranes were blocked in phosphate-buffered saline (PBS)–0.03% Tween 20 with 5% nonfat milk and probed with rabbit anti-FtsZ serum (29) diluted 1:10,000 in PBS–0.03% Tween 20 with 3% bovine serum albumin (BSA). Primary antibodies were detected using horseradish peroxidase-conjugated goat, anti-rabbit IgG (1:10,000; Sigma-Aldrich) and the enhanced-chemiluminescence (ECL) Western blotting reagent kit as described by the manufacturer (Thermo Scientific Pierce). For determination of the FtsZ cellular concentration, the intensity of the bands was quantified using ImageJ (http://imagej.nih.gov/ij/) and the recombinant pneumococcal FtsZ samples were used as the reference samples.

Conventional fluorescence microscopy image acquisition and analysis. Cells were grown at 37°C in CY to an OD_{600} of 0.3, transferred to microscope slides, and observed at room temperature using an Olympus BX61 optical microscope equipped with a UPFLN 100× O-2PH/1.3 ob-

jective and a QImaging Retiga-SRV 1394 cooled charge-coupled-device (CCD) camera. Images were acquired using the Volocity software package. Image analysis was performed using MicrobeTracker Matlab software (45).

PALM setup and acquisition method. *S. pneumoniae* cultures used for live- and fixed-cell imaging were grown at 37°C in CY depleted of riboflavin until an OD_{600} of 0.3 was reached. For live-cell imaging, cells were transferred to Gelzan (Sigma-Aldrich) pads containing C medium. For fixed-cell imaging, cells were fixed for 30 min at 20°C in the culture medium containing 2% paraformaldehyde and washed three times with PBS before transfer to thoroughly cleaned microscopy slides (Star-Frost; Light Labs.). We verified that these fixation conditions did not impair Z-ring functioning. First, we showed that *S. pneumoniae* cells grown at 37°C are able to divide without any lag time when placed on agarose or Gelzan pads at 20°C (Fig. S2A); second, we checked that all cells fixed under these conditions display a septal Z-ring (Fig. 2A); and third, we verified that Z-rings display similar features when cells are fixed at 37°C using 1% paraformaldehyde. For fixed-cell imaging, gravity was sufficient to obtain fields of immobile bacteria lying on the same focus plane at the surfaces of microscope slides. Images were acquired at 20°C with a home-built PALM setup based on an Olympus IX81 microscope (Olympus, Japan) and equipped with diode-pumped solid-state lasers at 405 nm (CrystaLaser), 488 nm (Spectra-Physics), and 561 nm (Cobolt, Jena). Wide-field illumination was achieved by focusing the circularly polarized laser beams to the back focal plane of a 100× 1.49-numerical-aperture (NA) oil immersion apochromatic objective lens (Olympus). The intensity and time sequence of laser illumination at the sample was tuned by an acousto-optical tunable filter (AOTF; Quanta Tech). To prevent sample drift during data acquisition, the samples were placed on an IX2-NPS nosepiece stage (Olympus) fixed directly on the objective. Fluorescence images were acquired with an Evolve back-illuminated electron micrograph CCD camera (Photometrics) controlled by the MetaMorph software (Molecular Devices). For PALM data collection, spDendra2 photoconversion was achieved at 405 nm by ramping up the power density from 1% to 100% of a typical maximum value of 14.4 $W \cdot cm^{-2}$, so as to counterbalance for the decrease of the available pool of nonphotoconverted molecules. Excitation of red photoconverted spDendra2 was performed at 561 nm with a typical power density of 8.8×10^3 $W \cdot cm^{-2}$ at beam center, which was adjusted so that most molecules were imaged and photobleached within 1 to 2 frames (Fig. S2D). Images were collected until photoconversion of spDendra2-FtsZ molecules became very infrequent, which usually happened after ~5,000 frames (Fig. S2C). To minimize autofluorescence induced by near-UV light illumination, PALM data sets were acquired using an alternate illumination scheme (Fig. S2B) consisting of 405-nm illumination periods of 21 ms (for fixed cells) or 10 ms (for live cells) for photoconversion, followed by 561-nm illumination readout periods of 30 ms or 15 ms for fixed and live cells, respectively.

General data processing and statistical analysis. All data processing was realized with Matlab (MathWorks). In order to test for statistical significance, *P* values were obtained by performing Student tests on all analyses. We set the significance level of our analyses to 1%.

PALM image reconstruction. Localizations of spDendra2-FtsZ molecules were determined by Gaussian least-squares fitting (26, 46). A mean localization precision of ~22 nm was typically found, and the detected photon budget per molecule was calculated to be ~420 photons/mol. Image rendering and molecular counting correcting for spDendra2 blinking was realized with homemade Matlab routines as described by Avilov et al. (26). Image rendering was realized by blurring each localization by convolution with a 2D Gaussian profile with the full width at half-maximum (FWHM) equal to the localization precision and by final binning with a pixel size of 8 nm. The spatial resolution of the reconstructed PALM images was estimated using the method of S. H. Shim et al. (47); the number of molecules (*N*) within segmented areas (*A*, typically Z-ring cross sections) was calculated, and the mean Nyquist resolution was given by $r \approx \langle 2/\sqrt{N/A} \rangle$. Using that method, and averaging over 56 Z-rings of cells at stage i, we found a resolution of ~38 nm.

Counting of imaged spDendra2 molecules. Molecular counting was performed according to the method described by Avilov et al. (26). Briefly, we corrected for spDendra2 blinking by using an upgraded version of the clustering optimization procedure proposed by Lee et al. (27), in which the photophysical behavior of spDendra2 was iteratively extracted from the experimental data itself. Under our experimental conditions, spDendra2 exhibited a photobleaching quantum yield of $\sim 2.6 \times 10^{-5}$, a blinking-off quantum yield of $\sim 7.4 \times 10^{-6}$, and a blinking-on rate of ~ 14.8 s^{-1}. Perhaps due to the specific environment encountered in *S. pneumoniae* cells, the blinking behavior of spDendra2 was found to be significantly reduced compared to that from our previous observations in mammalian cells (26). Of note, the number of imaged FtsZ-spDendra2 molecules was not significantly different when fixation was performed at 37°C using 1% paraformaldehyde.

Analysis of Z-ring geometry. Using MicrobeTracker, each cell was manually selected and oriented with the longitudinal cell axis parallel to the *x* axis. The pixel intensities along the *y* axis were then averaged and plotted against the *x* axis. Using a homemade Matlab script, the intensity plot was then fitted with a Gaussian function to measure the width at half-maximum of the peak, which was used as the axial thickness of the corresponding Z-ring.

PALM imaging simulation. Simulation of PALM imaging was performed as previously described (26), with the following modifications. 2D areas with dimensions corresponding to mean diameter and axial thickness values of the Z-ring imaged at stages i, ii, and iii of the cell cycle were designed under ImageJ. Using our Matlab-based simulation software (26), the experimental number of molecules imaged at each stage was randomly introduced into these 2D areas, with the same background levels as in the experiments. Simulation of the stochastic activation and imaging of these molecules were then performed as described in reference 26, and the simulated PALM image was reconstructed using the same scripts and parameters that were used to process experimental PALM data.

SUPPLEMENTAL MATERIAL

Supplemental material for this article may be found at http://mbio.asm.org/lookup/suppl/doi:10.1128/mBio.01108-15/-/DCSupplemental.

Text S1, PDF file, 0.1 MB.
Figure S1, TIF file, 1.1 MB.
Figure S2, TIF file, 1 MB.
Figure S3, TIF file, 1.4 MB.
Figure S4, TIF file, 2 MB.
Figure S5, TIF file, 0.9 MB.
Figure S6, TIF file, 0.5 MB.
Figure S7, TIF file, 2.8 MB.
Table S1, PDF file, 0.1 MB.

ACKNOWLEDGMENTS

This work used the platforms of the Grenoble Instruct center (ISBG; UMS 3518 CNRS-CEA-UJF-EMBL) with support from FRISBI (grant ANR-10-INSB-05-02) and GRAL (grant ANR-10-LABX-49-01) within the Grenoble Partnership for Structural Biology (PSB). Support for this work comes in part from the Agence Nationale de la Recherche (grants ANR-2011-BSV5-012-01 NOBLEACH and ANR-11-BSV8-005-01 PILIPATH) and the University of Grenoble Alpes. M.J. was funded by a Ph.D. grant from the Labex GRAL (Alliance Grenobloise pour la Biologie Structurale et Cellulaire Intégrées).

We thank M. Nollmann, D. Catoni, C. Grangeasse, T. Doan, and A. Zapun for useful discussions regarding PALM techniques and data. We are grateful to C. Grangeasse for providing us with the *ftsZ* Janus intermediate strain (*ftsZ-kan-rpsL*).

REFERENCES

1. **Löwe J, Amos LA.** 1998. Crystal structure of the bacterial cell-division protein FtsZ. Nature **391:**203–206. http://dx.doi.org/10.1038/34472.

2. **Li Z, Trimble MJ, Brun YV, Jensen GJ**. 2007. The structure of FtsZ filaments in vivo suggests a force-generating role in cell division. EMBO J **26:**4694–4708. http://dx.doi.org/10.1038/sj.emboj.7601895.
3. **Erickson HP, Anderson DE, Osawa M**. 2010. FtsZ in bacterial cytokinesis: cytoskeleton and force generator all in one. Microbiol Mol Biol Rev **74:**504–528. http://dx.doi.org/10.1128/MMBR.00021-10.
4. **Adams DW, Errington J**. 2009. Bacterial cell division: assembly, maintenance and disassembly of the Z ring. Nat Rev Microbiol **7:**642–653. http://dx.doi.org/10.1038/nrmicro2198.
5. **Egan AJ, Vollmer W**. 2013. The physiology of bacterial cell division. Ann N Y Acad Sci **1277:**8–28. http://dx.doi.org/10.1111/j.1749-6632.2012.06818.x.
6. **Lan G, Daniels BR, Dobrowsky TM, Wirtz D, Sun SX**. 2009. Condensation of FtsZ filaments can drive bacterial cell division. Proc Natl Acad Sci U S A **106:**121–126. http://dx.doi.org/10.1073/pnas.0807963106.
7. **Szwedziak P, Wang Q, Bharat TA, Tsim M, Löwe J**. 2014. Architecture of the ring formed by the tubulin homologue FtsZ in bacterial cell division. Elife **3:**e04601. http://dx.doi.org/10.7554/eLife.04601.
8. **Hsin J, Gopinathan A, Huang KC**. 2012. Nucleotide-dependent conformations of FtsZ dimers and force generation observed through molecular dynamics simulations. Proc Natl Acad Sci U S A **109:**9432–9437. http://dx.doi.org/10.1073/pnas.1120761109.
9. **Li Y, Hsin J, Zhao L, Cheng Y, Shang W, Huang KC, Wang HW, Ye S**. 2013. FtsZ protofilaments use a hinge-opening mechanism for constrictive force generation. Science **341:**392–395. http://dx.doi.org/10.1126/science.1239248.
10. **Osawa M, Anderson DE, Erickson HP**. 2008. Reconstitution of contractile FtsZ rings in liposomes. Science **320:**792–794. http://dx.doi.org/10.1126/science.1154520.
11. **Osawa M, Anderson DE, Erickson HP**. 2009. Curved FtsZ protofilaments generate bending forces on liposome membranes. EMBO J **28:**3476–3484. http://dx.doi.org/10.1038/emboj.2009.277.
12. **Meier EL, Goley ED**. 2014. Form and function of the bacterial cytokinetic ring. Curr Opin Cell Biol **26:**19–27. http://dx.doi.org/10.1016/j.ceb.2013.08.006.
13. **Ma X, Ehrhardt DW, Margolin W**. 1996. Colocalization of cell division proteins FtsZ and FtsA to cytoskeletal structures in living *Escherichia coli* cells by using green fluorescent protein. Proc Natl Acad Sci U S A **93:**12998–13003. http://dx.doi.org/10.1073/pnas.93.23.12998.
14. **Biteen JS, Goley ED, Shapiro L, Moerner WE**. 2012. Three-dimensional super-resolution imaging of the midplane protein FtsZ in live Caulobacter crescentus cells using astigmatism. Chemphyschem **13:**1007–1012. http://dx.doi.org/10.1002/cphc.201100686.
15. **Buss J, Coltharp C, Huang T, Pohlmeyer C, Wang SC, Hatem C, Xiao J**. 2013. In vivo organization of the FtsZ-ring by ZapA and ZapB revealed by quantitative super-resolution microscopy. Mol Microbiol **89:**1099–1120. http://dx.doi.org/10.1111/mmi.12331.
16. **Fu G, Huang T, Buss J, Coltharp C, Hensel Z, Xiao J**. 2010. In vivo structure of the E. coli FtsZ-ring revealed by photoactivated localization microscopy (PALM). PLoS One **5:**e12682. http://dx.doi.org/10.1371/journal.pone.0012680.
17. **Land AD, Tsui HC, Kocaoglu O, Vella SA, Shaw SL, Keen SK, Sham LT, Carlson EE, Winkler ME**. 2013. Requirement of essential Pbp2x and GpsB for septal ring closure in Streptococcus pneumoniae D39. Mol Microbiol **90:**939–955. http://dx.doi.org/10.1111/mmi.12408.
18. **Strauss MP, Liew AT, Turnbull L, Whitchurch CB, Monahan LG, Harry EJ**. 2012. 3D-SIM super resolution microscopy reveals a bead-like arrangement for FtsZ and the division machinery: implications for triggering cytokinesis. PLoS Biol **10:**e1001389. http://dx.doi.org/10.1371/journal.pbio.1001389.
19. **Holden SJ, Pengo T, Meibom KL, Fernandez C, Collier J, Manley S**. 2014. High throughput 3D super-resolution microscopy reveals Caulobacter crescentus in vivo Z-ring organization. Proc Natl Acad Sci U S A **111:**4566–4571. http://dx.doi.org/10.1073/pnas.1313368111.
20. **Zapun A, Vernet T, Pinho MG**. 2008. The different shapes of cocci. FEMS Microbiol Rev **32:**345–360. http://dx.doi.org/10.1111/j.1574-6976.2007.00098.x.
21. **Massidda O, Nováková L, Vollmer W**. 2013. From models to pathogens: how much have we learned about Streptococcus pneumoniae cell division? Environ Microbiol **15:**3133–3157. http://dx.doi.org/10.1111/1462-2920.12189.
22. **Fleurie A, Lesterlin C, Manuse S, Zhao C, Cluzel C, Lavergne JP, Franz-Wachtel M, Macek B, Combet C, Kuru E, VanNieuwenhze MS, Brun YV, Sherratt D, Grangeasse C**. 2014. MapZ marks the division sites and positions FtsZ rings in Streptococcus pneumoniae. Nature **516:**259–262. http://dx.doi.org/10.1038/nature13966.
23. **Tsui HC, Boersma MJ, Vella SA, Kocaoglu O, Kuru E, Peceny JK, Carlson EE, VanNieuwenhze MS, Brun YV, Shaw SL, Winkler ME**. 2014. Pbp2x localizes separately from Pbp2b and other peptidoglycan synthesis proteins during later stages of cell division of Streptococcus pneumoniae D39. Mol Microbiol **94:**21–40. http://dx.doi.org/10.1111/mmi.12745.
24. **Lutkenhaus J, Pichoff S, Du S**. 2012. Bacterial cytokinesis: from Z ring to divisome. Cytoskeleton (Hoboken) **69:**778–790. http://dx.doi.org/10.1002/cm.21054.
25. **Huang KH, Durand-Heredia J, Janakiraman A**. 2013. FtsZ ring stability: of bundles, tubules, crosslinks, and curves. J Bacteriol **195:**1859–1868. http://dx.doi.org/10.1128/JB.02157-12.
26. **Avilov S, Berardozzi R, Gunewardene MS, Adam V, Hess ST, Bourgeois D**. 2014. In cellulo evaluation of phototransformation quantum yields in fluorescent proteins used as markers for single-molecule localization microscopy. PLoS One **9:**e98362. http://dx.doi.org/10.1371/journal.pone.0098362.
27. **Lee SH, Shin JY, Lee A, Bustamante C**. 2012. Counting single photoactivatable fluorescent molecules by photoactivated localization microscopy (PALM). Proc Natl Acad Sci U S A **109:**17436–17441. http://dx.doi.org/10.1073/pnas.1215175109.
28. **Shaner NC, Campbell RE, Steinbach PA, Giepmans BN, Palmer AE, Tsien RY**. 2004. Improved monomeric red, orange and yellow fluorescent proteins derived from Discosoma sp. red fluorescent protein. Nat Biotechnol **22:**1567–1572. http://dx.doi.org/10.1038/nbt1037.
29. **Morlot C, Bayle L, Jacq M, Fleurie A, Tourcier G, Galisson F, Vernet T, Grangeasse C, Di Guilmi AM**. 2013. Interaction of penicillin-binding protein 2x and Ser/Thr protein kinase StkP, two key players in Streptococcus pneumoniae R6 morphogenesis. Mol Microbiol **90:**88–102. http://dx.doi.org/10.1111/mmi.12348.
30. **Morlot C, Zapun A, Dideberg O, Vernet T**. 2003. Growth and division of Streptococcus pneumoniae: localization of the high molecular weight penicillin-binding proteins during the cell cycle. Mol Microbiol **50:**845–855. http://dx.doi.org/10.1046/j.1365-2958.2003.03767.x.
31. **Fleurie A, Manuse S, Zhao C, Campo N, Cluzel C, Lavergne JP, Freton C, Combet C, Guiral S, Soufi B, Macek B, Kuru E, VanNieuwenhze MS, Brun YV, Di Guilmi AM, Claverys JP, Galinier A, Grangeasse C**. 2014. Interplay of the serine/threonine-kinase StkP and the paralogs DivIVA and GpsB in pneumococcal cell elongation and division. PLoS Genet **10:**e1004275. http://dx.doi.org/10.1371/journal.pgen.1004275.
32. **Lara B, Rico AI, Petruzzelli S, Santona A, Dumas J, Biton J, Vicente M, Mingorance J, Massidda O**. 2005. Cell division in cocci: localization and properties of the Streptococcus pneumoniae FtsA protein. Mol Microbiol **55:**699–711. http://dx.doi.org/10.1111/j.1365-2958.2004.04432.x.
33. **Puchner EM, Walter JM, Kasper R, Huang B, Lim WA**. 2013. Counting molecules in single organelles with superresolution microscopy allows tracking of the endosome maturation trajectory. Proc Natl Acad Sci U S A **110:**16015–16020. http://dx.doi.org/10.1073/pnas.1309676110.
34. **Durisic N, Laparra-Cuervo L, Sandoval-Álvarez A, Borbely JS, Lakadamyali M**. 2014. Single-molecule evaluation of fluorescent protein photoactivation efficiency using an *in vivo* nanotemplate. Nat Methods **11:**156–162. http://dx.doi.org/10.1038/nmeth.2784.
35. **Stricker J, Maddox P, Salmon ED, Erickson HP**. 2002. Rapid assembly dynamics of the Escherichia coli FtsZ-ring demonstrated by fluorescence recovery after photobleaching. Proc Natl Acad Sci U S A **99:**3171–3175. http://dx.doi.org/10.1073/pnas.052595099.
36. **Anderson DE, Gueiros-Filho FJ, Erickson HP**. 2004. Assembly dynamics of FtsZ rings in Bacillus subtilis and Escherichia coli and effects of FtsZ-regulating proteins. J Bacteriol **186:**5775–5781. http://dx.doi.org/10.1128/JB.186.17.5775-5781.2004.
37. **Chen Y, Erickson HP**. 2005. Rapid in vitro assembly dynamics and subunit turnover of FtsZ demonstrated by fluorescence resonance energy transfer. J Biol Chem **280:**22549–22554. http://dx.doi.org/10.1074/jbc.M500895200.
38. **Ester M, Kriegel H-P, Sander J, Xu X**. 1996. A density-based algorithm for discovering clusters in large spatial databases with noise. Proceedings of 2nd International Conference on Knowledge Discovery and Data Mining. Association for the Advancement of Artificial Intelligence (AAAI), Palo Alto, California, USA. https://www.aaai.org/Papers/KDD/1996/KDD96-037.pdf.

39. **Huang B, Jones SA, Brandenburg B, Zhuang X.** 2008. Whole-cell 3D STORM reveals interactions between cellular structures with nanometer-scale resolution. Nat Methods **5:**1047–1052. http://dx.doi.org/10.1038/nmeth.1274.
40. **Milam SL, Osawa M, Erickson HP.** 2012. Negative-station electron microscopy of inside-out FtsZ rings reconstituted on artificial membrane tubules show ribbons of protofilaments. Biophys J **103:**59–68. http://dx.doi.org/10.1016/j.bpj.2012.05.035.
41. **Holečková N, Doubravová L, Massidda O, Molle V, Buriánková K, Benada O, Kofroňová O, Ulrych A, Branny P.** 2015. LocZ is a new cell division protein involved in proper septum placement in Streptococcus pneumoniae. mBio **6**(1):e01700-14. http://dx.doi.org/10.1128/mBio.01700-14.
42. **Fleurie A, Cluzel C, Guiral S, Freton C, Galisson F, Zanella-Cleon I, Di Guilmi AM, Grangeasse C.** 2012. Mutational dissection of the S/T-kinase StkP reveals crucial roles in cell division of Streptococcus pneumoniae. Mol Microbiol **83:**746–758. http://dx.doi.org/10.1111/j.1365-2958.2011.07962.x.
43. **Sung CK, Li H, Claverys JP, Morrison DA.** 2001. An rpsL cassette, Janus, for gene replacement through negative selection in Streptococcus pneumoniae. Appl Environ Microbiol **67:**5190–5196. http://dx.doi.org/10.1128/AEM.67.11.5190-5196.2001.
44. **Lacks S, Hotchkiss RD.** 1960. A study of the genetic material determining an enzyme in Pneumococcus. Biochim Biophys Acta **39:**508–518.
45. **Sliusarenko O, Heinritz J, Emonet T, Jacobs-Wagner C.** 2011. High-throughput, subpixel precision analysis of bacterial morphogenesis and intracellular spatio-temporal dynamics. Mol Microbiol **80:**612–627. http://dx.doi.org/10.1111/j.1365-2958.2011.07579.x.
46. **Hess ST, Girirajan TP, Mason MD.** 2006. Ultra-high resolution imaging by fluorescence photoactivation localization microscopy. Biophys J **91:**4258–4272. http://dx.doi.org/10.1529/biophysj.106.091116.
47. **Shim SH, Xia C, Zhong G, Babcock HP, Vaughan JC, Huang B, Wang X, Xu C, Bi GQ, Zhuang X.** 2012. Super-resolution fluorescence imaging of organelles in live cells with photoswitchable membrane probes. Proc Natl Acad Sci U S A **109:**13978–13983. http://dx.doi.org/10.1073/pnas.1201882109.